Chapter 5

Innovative Techniques for 60-GHz On-Chip Antennas on CMOS Substrate

Adel T. Barakat, Ramesh K. Pokharel and
Hala A. Elsadek

Additional information is available at the end of the chapter

http://dx.doi.org/10.5772/66238

Abstract

The 60-GHz band has a 7-GHz of bandwidth enabling high data rate wireless communication. Also, it has a short wavelength allowing for passive devices integration into a chip, that is, fully integrated system-on-chip (SOC) is possible. This chapter features the design, implementation, and measurements of 60-GHz on-chip antennas (OCAs) on complementary-metal-oxide-semiconductor (CMOS) technology. OCAs are the primary barrier for the SOC solution due to their limited performance. This degraded performance comes from the low resistivity and the high permittivity of the CMOS substrate. We present here two innovative techniques to improve the CMOS OCAs' performance. The first method utilizes artificial magnetic conductors to shield the OCA electromagnetically from the CMOS substrate. The second methodology employs the PN-junction properties to create a high resistivity layer. Both approaches target the mitigation of the losses of the CMOS substrate; hence, the radiation performance characteristics of the OCAs are enhanced.

Keywords: CMOS, on-chip antenna (OCA), artificial magnetic conductor (AMC), distributed PN-junctions

1. Introduction

The millimeter wave band around the 60-GHz carrier has a broad bandwidth of 7 GHz and a short wavelength. This wide-ranging bandwidth allows for high data rate transmission of several gigabit-per-second (Gbps) suppressing the current low-frequency systems below 10 GHz. This excessive data rate opens the door for many applications such as high-speed video

and computer display streaming, Gbps networking, uncompressed high-definition media transfers, wireless personal area access, chip-to-chip communications, sensing applications, information showers, and virtually instantaneous admission to massive libraries of information. Moreover, an additional advantage of the 60-GHz carrier is the possibility of small-distance frequency reuse because of the high attenuation caused by oxygen molecules at the level of 10–15 dB/km. This frequency reuse attribute empowers the 60-GHz system to be an appropriate replacement for the contemporary short-range wireless communications systems. Additionally, the short free-space wavelength of 5 mm at 60 GHz enables small-size passive devices fabrication with integration capability into a chip. On-chip integration of passive devices leads to a wholly system-on-chip (SOC) realization. SOC is an individual and remarkable solution that can facilitate low-cost wireless communication devices. The SOC promotes the integration on the same chip of the antenna, front-end circuits, and back-end circuits. This SOC guarantees economical wireless communication devices thanks to the elimination of the costs associated with materials required for external antennas. Also, the antennas' matching circuits will be dismissed given that the 50-Ω boundary is no longer obligatory. Finally, SOC will guarantee a one-step foundry fabrication of the entire wireless system [1–16].

The cost-effective complementary-metal-oxide-semiconductor (CMOS) process, which is the mainstream digital circuits' technology, guarantees further cost reduction of the wireless system. Even though the CMOS substrate causes degradation of the radiation performance of the on-chip antennas (OCAs) due to its low resistivity and high permittivity [4–7], that is, the CMOS substrate is not optimized for the antennas operation. Many design methodologies have been utilized [4–12] to permit the improvement of the CMOS OCAs' performance. These OCAs' enhancement approaches have two main categories: (1) post-processing techniques [8–12] and (2) electromagnetic (EM) shielding [13–16].

Post-processing methods are techniques that utilize additional fabrication steps to the standard CMOS process to allow changing the characteristics of the CMOS substrate [8–12]. Micro-machining [8, 9] and proton implantation [10, 11] are two conventional CMOS post-processing methods. On the one hand, in the micro-machining approach, the OCA performance is enhanced by selectively removing parts of the CMOS substrate that lie directly below the OCA. Thus, the loss source is eliminated [8]. Wang et al. [8] had realized a peak measured gain and efficiency of 8 dBi and 60% by employing the selective etching technique together with array antenna at 130-GHz-operating frequency. Another micro-machining tactic uses post-supportive micro-machined walls to isolate the OCA far apart from the CMOS substrate [9]; hence, the coupling between the OCA and the substrate reduces and its radiation performance is enhanced. Kim et al. [9] had achieved a peak simulated gain and efficiency of 9.9 dBi and 94%, respectively by using this post-supportive walls method with patch antenna array at 60-GHz-operating frequency.

On the other hand, the proton implantation course implements high-energy ions into the CMOS substrate below the OCA such that the CMOS substrate's resistivity below the OCA becomes very high, the corresponding losses are reduced, and the OCA's performance is enhanced [10, 11]. In Ref. [10], proton implantation increased the CMOS substrate resistivity

http://dx.doi.org/10.5772/66238

from [22] 10 Ω.cm to 0.1 MΩ.cm. In return, the transmission gain is enriched by 20 dB. In Ref. [11], a helium-3 ion irradiation process is applied to reduce the substrate losses of the OCA. Therefore, the radiation efficiency of the OCA is doubled, and a measured peak gain of -4.1 dBi is possible at 60 GHz. However the possibility of high performance using the post-processing techniques, these techniques have two major disadvantages: (1) the extra costs associated with them due to the additional fabrication steps and (2) the repeatability of the fabrication process [12].

Alternatively, the EM shielding uses the standard CMOS technology without any further processing. The EM shielding employs artificial magnetic conductors (AMCs) to enhance OCA radiation performance such as gain and radiation efficiency [12–16]. In Ref. [13], Chu et al. implemented a wide band patch OCA with two parasitic patches and used a snowflake AMC as a shield. However the wide bandwidth, this design had shown low gain and low efficiency of -2.2 dBi and 15%, respectively. Barakat et al. [14, 15] designed a triangular patch OCA over Jerusalem-Cross (JC) [14] and square [15] AMC. A methodology to enhance gain and efficiency while maintaining small area is also proposed [14, 15]. In this methodology, gain and efficiency have been enhanced by increasing the number of AMC cells in the E-plane direction and reducing the number of AMC cells in the H-plane direction. A simulated gain and efficiency of 0 dBi and 39%, respectively, were observed for JC-AMC [14] and 0.7 dBi and 47%, respectively, for square-AMC [15]. Bao et al. [16] has proposed a double-loop OCA with modified star AMC. The double-loop OCA originally has circular polarization. When using full AMC layer below the double loop, the axial ratio bandwidth is reduced due to the coupling between the OCA and the AMC cells. To overcome this problem, Bao et al. [16] proposed selectively removing some cells from the AMC plan to maintain a wide axial-ratio bandwidth while efficiency is enhanced. An AR bandwidth (AR <3) was possible from 57 to 67 GHz with a peak measured gain of -4.4 dBi [16]. The AMC-based OCAs still have poor measured performance when compared to the post-processed OCAs [8–16].

This chapter presents the design, implementation, and measurements of the 60-GHz CMOS OCAs. We propose two innovative techniques to advance the CMOS OCAs' performance. The first method uses electromagnetic shielding employing asymmetric AMC. The OCAs based on the asymmetric AMC is superior in the gain-to-active-area ratio when compared to the OCAs making use of the traditional symmetric AMC as will be detailed in Section 2. The second scheme is the distributed N-well method. In this distributed N-well approach, the semiconductor physics characteristics of the PN-junction (PNJ) are utilized to consent the increase of the effective resistance of the CMOS substrate, hence, reducing the resulting losses and the OCA's performance enhances. This chapter describes the distributed N-well tactic and its application to OCA's performance boosting in Section 3.

2. OCA with asymmetric AMC

In this section, we report the use of asymmetric AMC to enhance the performance of the OCA. First, in Section 2.1, we detail the background of the AMCs showing their importance in

antenna engineering applications. Then, we discuss the development of the asymmetric AMC from the traditional symmetric AMC in Section 2.2. Furthermore, in Section 2.3, we manipulate the symmetric and the asymmetric AMC in the OCA's characteristics progression, comparing the resulting performances. Then, we detail the layout and fabrication consideration, the measurements technique used, and the measured data of the OCA with asymmetric AMC in Section 2.4.

2.1. History of AMC

An AMC layer consists of periodic metal patches over a dielectric substrate in one-, two-, or three-dimensional (3D) configurations. AMC surfaces have two important and exciting properties that do not occur naturally and benefit a variety of microwave circuit applications. These two AMC individualities are the high impedance and the in-phase reflection properties. First, an AMC surface acts as a high-impedance layer that is useful as an antenna ground plane regarding surface-wave suppression. AMC shields have very high-surface impedances within an explicitly narrow frequency band, where the tangential magnetic field intensity is small, even with a large electric field intensity along the surface [17, 18]. Second, an AMC has an unusual reflection phase (RP) features of 0° at its center frequency; hence, an antenna on AMC produces a smoother radiation profile than a similar antenna on a conventional metallic ground plane, with less power wasted in the backward direction. These AMC capabilities are useful to the diversity of antenna schemes, for example, patch antennas, that frequently suffer from the consequences of surface waves propagation. For phased arrays, the suppression of the surface waves can reduce the mutual coupling between the array elements; hence, it helps to eliminate the blind-scanning angles.

Furthermore, an AMC is particularly applicable to the field of portable hand-held communication devices, in which the interaction between the antenna and the user can have a significant impact on both the antenna's performance and the user's health. An AMC acting as a shield between the antenna and the user in portable communications equipment can lead to a higher antenna efficiency, a longer battery life, a lower specific absorption rate (SAR) of the human body, and a lighter device weight. Likewise, in the case of OCA, an AMC surface is placed between the antenna and the lossy CMOS substrate. Consequently, the AMC surface allows for better OCA's efficiency [13–18]. The reflection phase is the ratio between the phase of the reflected electric field and the phase of the incident electric field at the reflecting surface. In practice, the AMC plane exhibits a reflection coefficient of +1 at its center frequency and thus the reflected wave can constructively enhance the total electromagnetic field with the incident wave together at a low profile. On the contrary, the conventional perfect electrical conductor (PEC) plan delivers a reflection coefficient of -1 and therefore the reflected wave will destructively cancel the incident signal for low-profile operation.

The reflection phase on the AMC plane varies with the frequency continuously from -180° to 180° and become zero at the center-operating frequency. The operational band of an AMC layer is the range for which the reflection phase changes from +90° to -90°, as in this bandwidth, the reflection phase values would not cause destructive interference between the direct and the reflected waves. Following this definition of the reflection phase, the AMC percentage

http://dx.doi.org/10.5772/66238

bandwidth (BW_{AMC}) can be calculated as in Eq. (1) [13–18], where f_h is the frequency at which the reflection phase equals -90°, f_{lo} is the frequency at which the reflection phase equals 90°, and f_c is the center frequency at which the reflection phase equals 0°.

$$\mathrm{BW}_{\mathrm{AMC}} = \frac{f_h - f_{lo}}{f_c} \times 100\% \tag{1}$$

2.2. Development of the asymmetric rectangular AMC-based OCA

2.2.1. Symmetric square AMC

Figure 1(a) shows two consecutive unit cells of the symmetric square AMC [15, 19]. We used the high-frequency-structure-simulator (HFSS) to optimize the reflection phase (RP) response of this AMC and for other simulations in this chapter. **Figure 1(b)** shows the simulation setup to determine the square AMC's RP response. Perfect-E and perfect-H boundary conditions are used to realize the periodic boundary conditions (PBCs). Excitation port is a wave port. We embed the reflection coefficient (S11) in the surface of the AMC unit cell and compute the RP response as the angle of the embedded S11. A percentage bandwidth of 16.5% is achieved for the dimensions d = 260 μm and g = 30 μm as shown in **Figure 1(c)**.

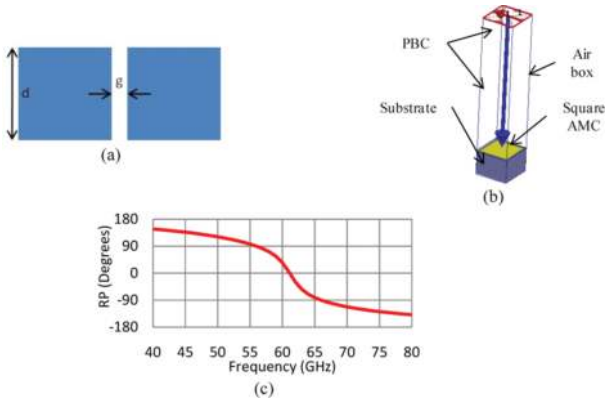

Figure 1. Two consecutive unit cells of square AMC. (b) HFSS simulation setup. (c) Reflection phase (RP) of the square AMC with d = 260 μm and g = 30 μm. "Reprinted with permission from Microwave Journal."

2.2.2. Asymmetric rectangular AMC

A transverse-magnetic (TM) wave with its electric field (E-field) directed in the YZ-plan and magnetic field (H-field) propagating in the x-direction incident on a "Cohn square" in free space [20] is shown in **Figure 2(a)**. For this TM wave, no detected E-field on the square AMC's plan appears in the space between the edges parallel to the y-direction. Thus, the square AMC reduces to a strip array of asymmetric rectangular AMC as shown in **Figure 2(b)** [21].

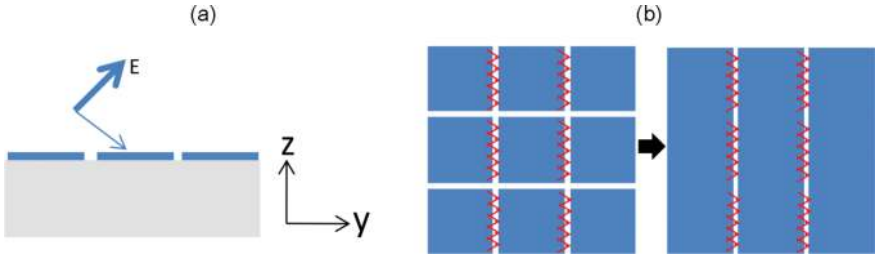

Figure 2. Square AMC with incident TM wave polarized in the *YZ*-plan. (b) Original and equivalent AMC structures at *XY*-plan. "Reprinted with permission from Microwave Journal."

2.2.3. Circular OCA over AMC

The AMCs presented in Sections 2.2.1, and 2.2.2 are utilized to enhance the radiation characteristics of a circular OCA. First, the methodology presented in [14, 15] is maintained to guarantee high gain-to-active-area ratio. According to this method, a high gain-to-active-area ratio is possible by increasing the number of AMC cells in the direction of the antenna polarization and decreasing them at the normal to this direction. **Figure 3(a)** and **(b)** shows a top view and three-dimensional (3D) view of the OCA employing square AMC, respectively. **Figure 3(c)** displays a top view of the circular OCA on rectangular AMC. We designed the two structures (OCA on square AMC and OCA on rectangular AMC) with the dimensions listed in **Table 1**, and they have the same chip area of 840 × 1710 μm^2.

Also, the two structures have a high agreement in the matching performance, gain and efficiency responses, and current distribution as can be interpreted from **Figure 3(d)** and **(f)**, respectively. The simulated gain and radiation efficiency are -0.8 dBi and 22.5%, respectively, at 60 GHz. These observations in **Figure 3** stand as an additional proof that the symmetric square AMC and asymmetric rectangular AMC are equivalent for TM mode antennas.

2.2.4. Circular OCA over modified asymmetric AMC

In the previous sections from 2.2.1 to 2.2.3, we have demonstrated that TM-mode circular OCA, which is exploiting the symmetric square AMC, and the asymmetric rectangular AMC undergo similar performances regarding impedance matching and radiation characteristics such as gain and efficiency. In this section, we detail how the asymmetric rectangular AMC can be modified such that the gain-to-active-area ratio can increase. **Figure 4(a)** shows the circular OCA over a modified asymmetric AMC. We applied the following adjustments to the asymmetric AMC:

Removing the two AMC cells that lay directly below the OCA in **Figure 3(c)**. Bao et al. [16] originally proposed this AMC cells removal for peak gain and axial ratio bandwidth boosting.

http://dx.doi.org/10.5772/66238

Limiting the length (L) of the modified AMC unit cell from 860 to 710 μm since in this direction the gain performance is negligibly affected as pointed in [14, 15]. Also, the gap "g" between each of the remaining consecutive cells is reduced to 5 μm.

Adding circular rounds to the AMC cells near to the OCA as shown in **Figure 4(a)** and then adjusting the separation between the OCA and the modified AMC cells with circular rounds "d1" and the separation between the modified AMC cells with circular rounds "d2."

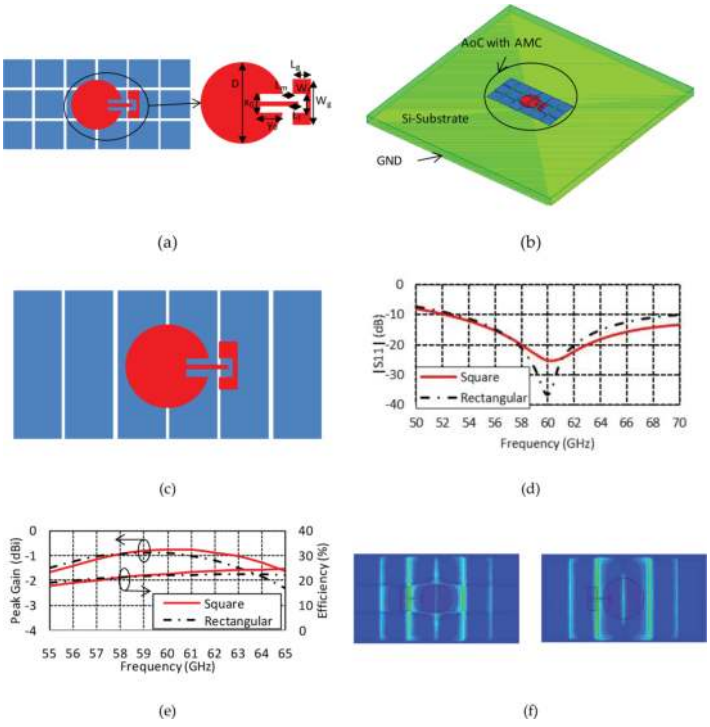

Figure 3. Top view of circular OCA over square AMC. (b) 3D view of circular OCA over square AMC. (c) Top view of circular OCA over rectangular AMC. (d) Simulated |S11| comparison. (e) Simulated peak gain and efficiency comparison. (f) Simulated current distribution comparison (left: square AMC; right: rectangular AMC) "Reprinted with permission from Microwave Journal."

D	x_0	y_0	L_m	W_m	L_f	W_f	L_g	W_g
450	64	85	60	14	50	54	100	254

Reprinted with permission from Microwave Journal.

Table 1. Optimized dimensions of circular OCA employing square AMC.

By applying the above modifications to the asymmetric rectangular AMC, the resulting OCA over modified asymmetric AMC establishes a gain of 0 dBi at 60 GHz within a chip area of 1.19 mm^2. The design dimensions are the same as in **Table 1** except x_0 = 44 μm and y_0 = 100 μm. The values of x_0 and y_0 are changed to adjust impedance matching. Besides, this OCA over modified asymmetric AMC has a 0.8-dB higher gain than that of the OCA over square/rectangular AMCs described in Section 2.2.3 while the chip area of this OCA reduces from 840 × 1710 to 710 × 1710 μm^2 (by more than 17%). **Figure 4(b)** presents the simulated |S11| and peak gain responses of the OCA over modified asymmetric AMC. Moreover, this OCA is matched (|S11|<-10 dB) from 52 GHz until above 70 GHz covering the bandwidth of interest around the 60-GHz carrier.

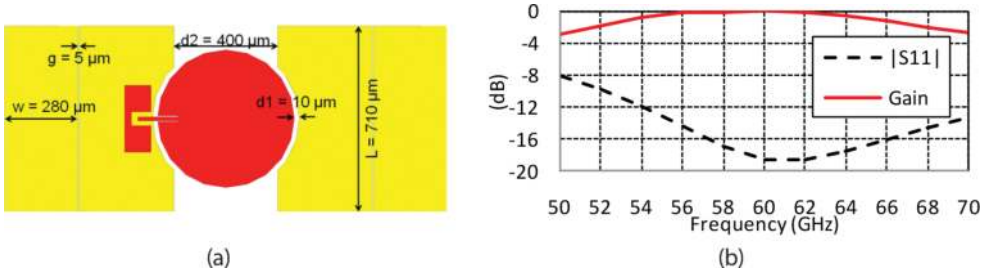

Figure 4. Circular OCA over modified asymmetric AMC: (a) top view and (b) simulated |S11| and peak gain. "Reprinted with permission from Microwave Journal."

3. OCA with distributed N-well grid

In Section 2, the chapter focused on enhancing the gain-to-active-area ratio by employing a modified asymmetric AMC EM shield. Otherwise, this section presents a different procedure based on the semiconductor properties of the PN-junction (PNJ) to improve this ratio. A PNJ creation results from the coexistence of the P and N semiconductor types. A depletion layer, which is carriers' free area, will appear between the two semiconductors' types [22, 23]. Subsequently, in this section, we employ this depletion layer concept in the OCA's gain-to-active-area ratio enrichment, as will be clarified in the following sections.

3.1. Large depletion layer formation

A PNJ is described by its built-in voltage (V_i) and depletion width (x_d) which can be computed by Eq. (2) and Eq. (3), respectively, where, K is Boltzmann constant, T is temperature, q is electron's charge, N_a and N_d are acceptors and donors doping concentrations in P-type and N-type, respectively, while n_i and ε_s are intrinsic doping and permittivity of the silicon, respectively, and V_a is bias voltage applied on the PNJ [22, 23]. The width of depletion on the P-type (x_P) and N-type (x_N) semiconductors can be computed as Eq. (4) [22, 23].

http://dx.doi.org/10.5772/66238

$$V_i = \frac{KT}{q} \ln\left(\frac{N_a N_d}{n_i^2}\right) \tag{2}$$

$$x_d = \sqrt{\frac{2\varepsilon_s}{q}\frac{N_a + N_d}{N_a N_d}\left(V_i - V_a\right)} \tag{3}$$

$$x_P = x_d \frac{N_d}{N_d + N_a} \qquad x_N = x_d \frac{N_a}{N_d + N_a} \tag{4}$$

Typically, a depletion area will be in the range of a few micrometers. However, we achieved a large depletion area by distributing N-type semiconductor within the P-type semiconductor in a manner for which all the targeted area has depleted. **Figure 5** reveals how this criterion is possible. In **Figure 5(a)**, rectangular-shaped N-type semiconductor cells are spread within the P-type with a cell width of $2x_N$ and each of the two sequential cells is separated by $2x_P$ [23]. These values are selected to deplete the formed two PNJs.

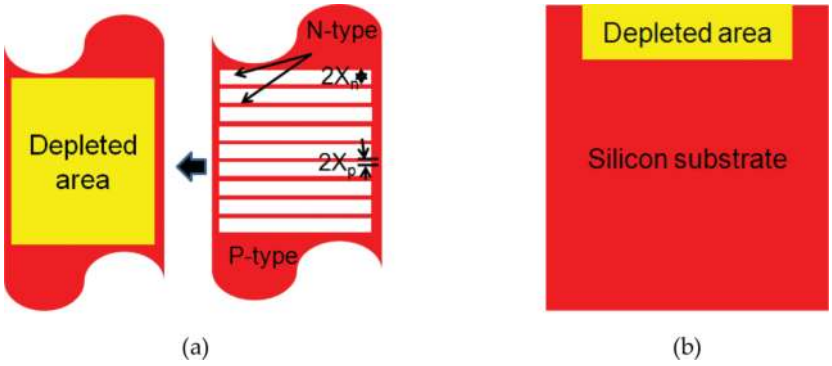

Figure 5. (a) Grid of rectangular-shaped N-type semiconductor on a P-type semiconductor with dimensions that satisfy full depletion condition and its equivalent depleted area. (b) Side view of the depleted region [23].

3.2. Gain-to-active-area ratio improvement using large depletion layer

As shown in **Figure 6(a)**, we have implemented the outsized depletion area below the OCA. This OCA is originally the OCA on modified asymmetric AMC shown in **Figure 4(a)**. The depletion layer has the same dielectric constant as silicon (ε_r = 12), and we modeled its conductivity as σ = 0.1 S/m, representing a very low loss. The depletion depth (t = 20 μm) is equal to the typical height of the N-type material (N-well) in the 0.18-μm CMOS process [23].

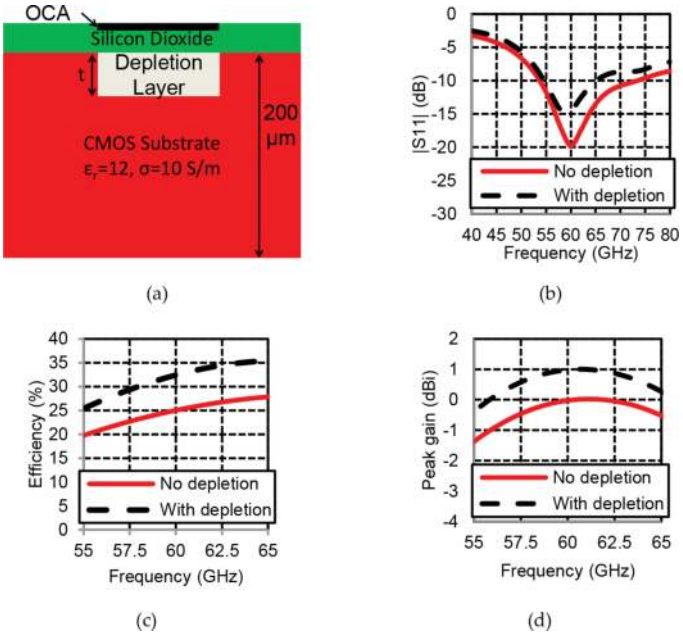

Figure 6. Simulation comparison of the OCA with/without depletion layer below (a) cross-sectional view of the OCA with the depletion zone, (b) |S11|, (c) efficiency, and (d) peak gain [23].

Hereafter, we compare the simulated performance of the OCA on modified AMC with/without depletion area in terms of |S11|, radiation efficiency, and peak gain as shown in **Figure 6(b)–(d)**, respectively. Both OCAs with/without depletion demonstrate a matched response (|S11|<-10 dB) at the bandwidth of interest around 60 GHz. Besides, the existence of the depletion layer leads to the improvement of the radiation efficiency and the peak gain of the OCA. The radiation efficiency is increased at 60 GHz from 25 to 32% as shown in **Figure 6(c)**. Moreover, the peak gain at 60 GHz is improved from 0 to 1 dBi as illustrated in **Figure 6(d)**. The optimized design dimensions of the OCA with depletion layer are similar to the one without depletion layer except x_0 = 44 μm [23].

4. Layout, fabrication, and measurements

4.1. Layout and fabrication

The 0.18-μm CMOS technology used is a TSMC six-metal process. These process six metals are denoted as M1–M6 from bottom to top. The top metal layer "M6" is selected for the circular OCA implementation and its feeding microstrip line for two reasons. First, it has the largest thickness and then it has lower conduction losses than the other metal layers (M1–M5). Second, M6 layer has the highest separation from the lossy CMOS substrate; hence, it should have the

http://dx.doi.org/10.5772/66238

least coupling with the CMOS substrate and the lowest power leakage to it [19, 23]. The other metal layers (M1–M5) are used for the construction of the modified asymmetric AMC. We illustrate the specific layout tips in the following paragraph.

The HFSS and Cadence Virtuoso layouts of the circular OCA on modified asymmetric AMC plan are shown in **Figure 7(a)** and **(b)**, respectively. Also, a photograph of the fabricated OCA is provided in **Figure 7(c)**. We performed a slight change in the feeding position. The modification in the feeding topology targeted the compensation of the measuring pads' low impedance and capacitive nature. The pads' coplanar waveguide (CPW) grounds at M6 are connected using via connections to M1 "the AMC unit cell." Moreover, to fulfill design rules of the TSMC 0.18-μm CMOS process, the design has the following alternations:

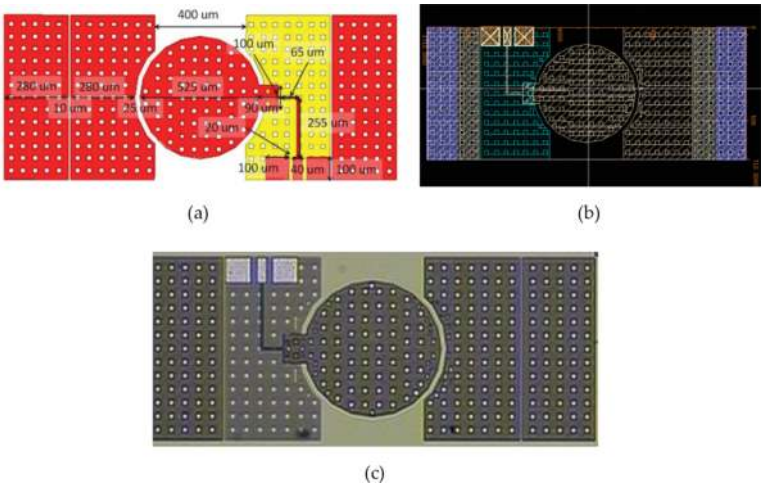

Figure 7. (a) OCA layout at HFSS with dimensions. (b) OCA layout at Cadence Virtuoso. (c) Fabricated OCA.

Minimum density design rule: The two AMC cells far from the circular radiator are redesigned to be composed of a stacked metal from layer 1 (M1) to layer 6 (M6). Also, a layer of polysilicon is included below these AMC cells to fulfill the same purpose. Then, the design is resimulated, and some dimensions are adjusted as shown in **Figure 7(a)** to confirm no/slight effect in performance.

Maximum metal width design rule: 20-μm × 20-μm rectangle slots are etched from all of the metals. These slots' sizes were selected considering that they resonate far beyond the 60-GHz band.

4.2. Measurements

The measurements are performed using a VNA (E8361C PNA 10 MHz to 67 GHz) and a Cascade Microtech manual probe station. A Cascade Microtech calibration kit with part

number "101-190" allowed the ground-signal-ground (GSG) short-open-load-through (SOLT) Calibration for the infinity probe used to measure the |S11| of the fabricated OCAs.

Figure 8 shows the measured matching and gain performance of the OCAs without depletion. This OCA exhibits a matched behavior (|S11|<-10 dB) at the bandwidth of interest with good agreement with the simulated |S11| as shown in **Figure 8(a)**. Also, it has a measured gain of -3 dB at 64 GHz as shown in **Figure 8(b)**. The OCA with depletion area below has the same layout as in **Figure 7** except that it has an additional grid of N-well (N-type material) with width of $2x_n$ = 0.86 μm and separated by $2xp$ = 1.4 μm on the P-type substrate to guarantee the depletion layer formation. The measured |S11| of this antenna is in fair agreement with the simulated performance as shown in **Figure 9**. This OCA underdoes a peak gain of -1.5 dB at 66 GHz. The discrepancy in the gain performances is due to nearby metals, probe pins, and probe body which are not considered in simulations [19, 23]. The OCA with depletion has a 1.5 dB higher gain than that without depletion layer.

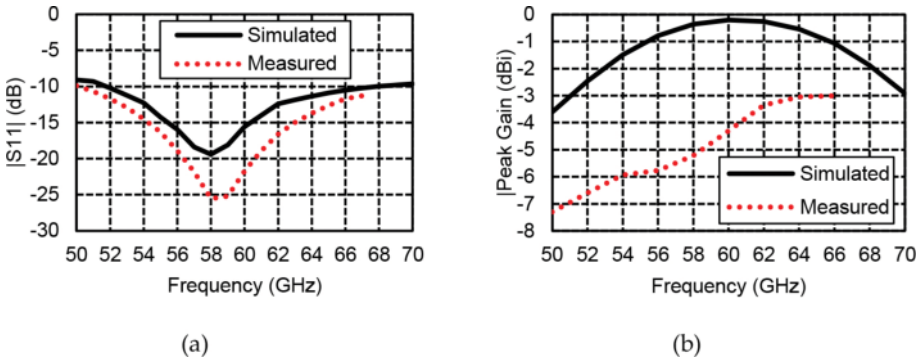

Figure 8. The simulated and measured performances of the OCA on modified AMC without depletion (a) |S11| and (b) peak gain.

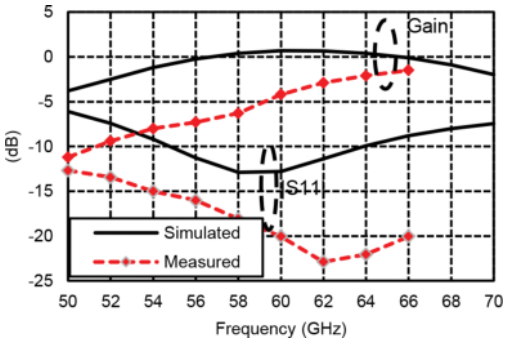

Figure 9. Simulated and measured performance of the OCA with depletion (t = 20 μm) [23].

http://dx.doi.org/10.5772/66238

We used a simple setup based on the reference antenna gain method [24] for the OCA peak gain measurements shown in **Figure 8(b)** and **Figure 9**. First, we performed a VNA insertion loss response calibration by placing a two V-band standard gain horn (SGH) antennas separated by 1 m to calibrate all losses caused by including cables and free-space path loss. Second, the target OCA replaced the receiving SGH while keeping the same measuring distance between the two antennas, and insertion loss ($S_{21_{calibrated}}$) is measured again. Finally, we calculate the OCA gain (G_{OCA}) using Eq. (5), where L_{probe} is losses of feeding infinity® GSG probe and G_{SGH} is receiving SGH antenna gain.

$$G_{OCA} = S_{21calibrated} + L_{probe} + G_{SGH} \tag{5}$$

To enable the measurement of the OCA efficiency and radiation pattern, we used the advanced setup described in [25]. A photograph of the measurement setup is shown in **Figure 10(a)**. For correct handling, the OCA is placed using supporting foam which is mostly invisible to the EM waves as shown in **Figure 10(b)**. A piece of metal is placed below the chip to realize the package ground. We used this setup to characterize the OCA without depletion shown in **Figure 7(c)**. The measured |S11| is in good agreement with the simulated |S11| and is identical to that in **Figure 8(a)** which was measured on probe station.

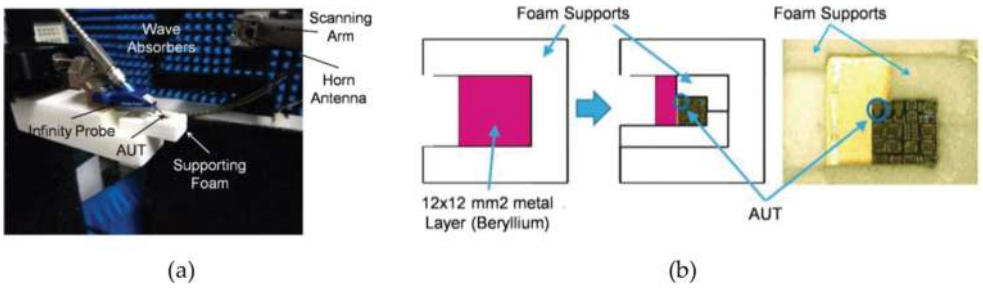

Figure 10. (a) Measurement setup. (b) Visualization of the measurements support structure. "Reprinted with permission from Microwave Journal."

The measured peak gain has a discrepancy of up to 4 dB when compared to the simulated one as shown in **Figure 11(a)**. This inconsistency resulted from the other fabricated structures surrounding the OCA, the probe pins, and the probe body which are not considered in simulations. So, we performed additional simulations to validate these gain measurements. In **Figure 11(b)**, we show another simulation model which we used in this validation. This model considers the nearest fabricated structures which may affect the OCA performance. Using this model, the simulated peak gain noted as "With metals" in **Figure 11(a)** is in fair agreement with the measured results especially for frequencies up to 58 GHz. Other discrepancies between measured and simulated gain may be due to other metals which are not modeled, and also due to the ±0.8-dB accuracy of the measurement setup [25].

Finally, we present the measured E-plane and H-plane radiation patterns at 56, 60, and 64 GHz in **Figure 12**. The E-plane and H-plane are located at *XZ*- and *XY*-cut planes, respectively. The radiation patterns are in fair agreements. However, these radiation patterns show some twist especially for the E-plane.

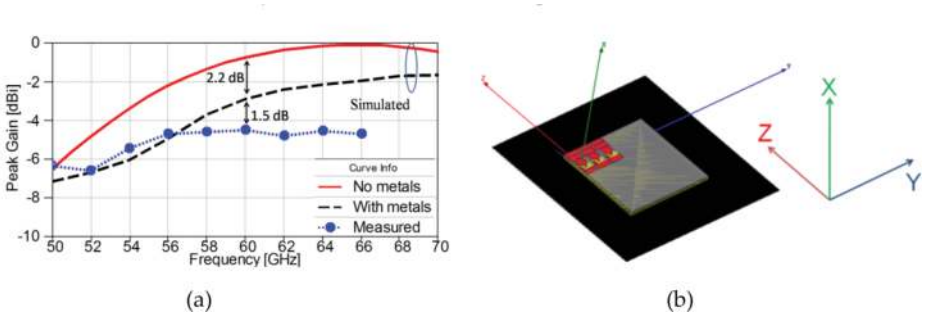

Figure 11. (a) Measurement results using the setup in Ref. [25]. (b) HFSS model for measurement validation. "Reprinted with permission from Microwave Journal."

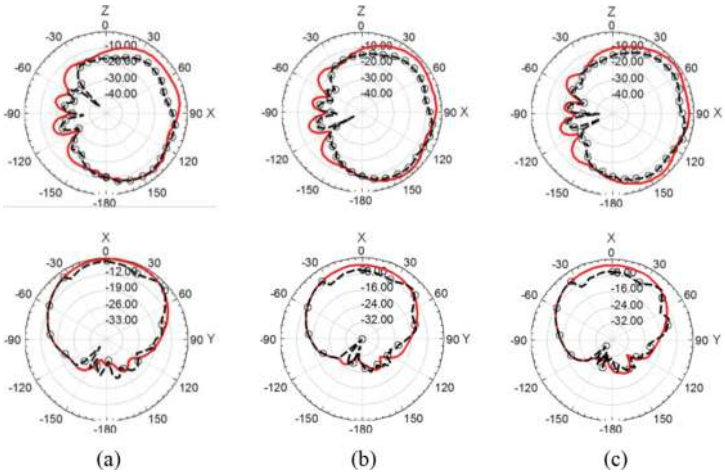

Figure 12. E-plane (top) and H-plane (down) radiation patterns at (a) 56GHz, (b) 60GHz, and (c) 64GHz. Measured (dashed) and simulated (solid). "Reprinted with permission from Microwave Journal."

5. Conclusions

We have presented in this chapter two unconventional distinct techniques to improve the OCAs' performance on CMOS technology regarding a high gain-to-active-area ratio. The first

http://dx.doi.org/10.5772/66238

technique extended the concept of EM shielding using asymmetric AMC, then modified asymmetric AMC. The OCA based on modified asymmetric AMC realized a peak gain of -4 dBi within a chip area of 1.21 mm^2. The second technique employed the PNJ depletion concept to form a large area of low loss. The OCA on modified asymmetric AMC and large depletion area showed a gain of -1.5 dBi on the same area of 1.21 mm^2. The measured gain performances were lower than that predicted by simulation due to the sensitivity of the OCAs to the surrounding chip environment.

Acknowledgements

The authors like to thank Prof. H. Kanaya of Kyushu University, Fukuoka, Japan, and Prof. R. Suga of Aoyama Gakuin University, Tokyo, Japan, for their support in the initial measurements. The authors are grateful for Prof. C. Luxey and Mr. A. Bisognin of the University of Nice Sophia-Antipolis, Nice, France, for performing the complete measurements of the OCA on modified asymmetric AMC. A part of this work is supported by a Grant-in-Aid for Scientific Research (C) (16K06301), and VLSI Design and Education Center partially (VDEC), the University of Tokyo in collaboration with CADENCE and Keysights Corporations.

Author details

Adel T. Barakat[1,2], Ramesh K. Pokharel[1*] and Hala A. Elsadek[2]

*Address all correspondence to: pokharel@ed.kyushu-u.ac.jp

1 Kyushu University, Fukuoka, Japan

2 Electronics Research Institute, Cairo, Egypt

References

[1] Hansen C. J., WIGIG: multi-gigabit wireless communications in the 60 GHz band. IEEE Wireless Communications Magazine. 2011;18(6):6–7. DOI: 10.1109/MWC.2011.6108325

[2] Singh H., Oh J., Kweon C., Qin X., Shao H-R, and Ngo C., A 60 GHz wireless network for enabling uncompressed video communication. IEEE Communications Magazine. 2008;47(12):71–78. DOI: 10.1109/MCOM.2008.4689210

[3] Rappaport T. S., Murdock J. N., and Gutierrez F., State of the art in 60-GHz integrated circuits and systems for wireless communications. Proceedings of the IEEE. 2011;99(8): 1390–1436. DOI: 10.1109/JPROC.2011.2143650

[4] Zhang Y. P., Sun M., and Guo L. H., On-chip antennas for 60-GHz radios in silicon technology. IEEE Transactions on Electron Devices. 2005;52(7):1664–1668. DOI: 10.1109/TED.2005.850628

[5] Hsu S. S., Wei K. C., Hsu C. Y., and Ru-Chuang H., A 60-GHz millimeter-wave CPW-fed yagi antenna fabricated by using 0.18-um CMOS technology. IEEE Electron Device Letters. 2008;29(6):625–627. DOI: 10.1109/LED.2008.920852

[6] Lin C. C., Hsu S. S., Hsu C. Y., and Chuang H. R., A 60-GHz millimeter-wave CMOS RFIC-on-chip triangular monopole antenna for WPAN applications. In: IEEE Antennas and Propagation Society International Symposium; 9–15 June 2007; Honolulu, HI, USA. USA: IEEE; 2007. p. 2522–2525. DOI: 10.1109/APS.2007.4396047

[7] Guo P. J. and Chuang H. R., A 60-GHz millimeter-wave CMOS RFIC-on-chip meander-line planar inverted-F antenna for WPAN applications. In: IEEE Antennas and Propagation Society International Symposium; 5–11 July 2008; San Diego, CA, USA. USA: IEEE; 2008. p. 1–4. DOI: 10.1109/APS.2008.4619464

[8] Wang R., Sun Y., Kaynak M., Beer S., Borngräber J., and Scheytt J. C., A micromachined double-dipole antenna for 122–140 GHz applications based on a SiGe BiCMOS technology. In: IEEE International Microwave Symposium Digest; 17–22 June 2012; Montreal, QC, Canada. USA: IEEE; 2012. p. 1–3. DOI: 10.1109/MWSYM.2012.6258421

[9] Kim J-G. , Lee H. S., Lee H-S., Yoon J-B., and Hong S., 60-GHz CPW-fed post-supported patch antenna using micromachining technology. IEEE Microwave and Wireless Components Letters. 2005;15(10):635–637. DOI: 10.1109/LMWC.2005.856690

[10] Rashid A. B. M. H., Watanabe S., and Kikkawa T., High transmission gain integrated antenna on extremely high resistivity Si for ULSI wireless interconnect. IEEE Electron Device Letters. 2002;23(12):731–733. DOI: 10.1109/LED.2002.805754

[11] Wu R. et al., A 60-GHz efficiency-enhanced on-chip dipole antenna using helium-3 ion implantation process. In: 44th European Microwave Conference; 6–9 October 2014; Rome, Italy. USA: IEEE; 2014. p. 108–111. DOI: 10.1109/EuMC.2014.6986381

[12] Cheema H. M. and Shamim A., The last barrier: on-chip antennas. IEEE Microwave Magazine. 2013;14(1):79–91. DOI: 10.1109/MMM.2012.2226542

[13] Chu H., Guo Y. X., Lin F., and Shi X. Q., Wideband 60GHz on-chip antenna with an artificial magnetic conductor. In: 2009 Radio-Frequency Integration Technology; 9–11 December 2009; Singapore. USA: IEEE; 2009. p. 307–310. DOI: 10.1109/RFIT.2009.5383667

[14] Barakat A., Allam A., Pokharel R. K., Elsadek H., El-Sayed M., and Yoshida K.,Performance optimization of a 60 GHz antenna-on-chip over an artificial magnetic conductor. In: 2012 Japan-Egypt Conference on Electronics, Communications, and Computers; 6–9 March 2012; Alexandria, Egypt. USA: IEEE; 2012. p. 118–121. DOI: 10.1109/JEC-ECC.2012.6186968

[15] Barakat A., Allam A., Pokharel R. K., Elsadek H., El-Sayed M., and Yoshida K., 60 GHz triangular monopole antenna-on-chip over an artificial magnetic conductor. In: 6th European Conference on Antennas and Propagation; 26–30 March 2012; Prague, Czech Republic. USA: IEEE; 2012. p. 972–976. DOI: 10.1109/EuCAP.2012.6206127

[16] Bao X. Y., Guo Y. X., and Xiong Y. Z., 60-GHz AMC-based circularly polarized on-chip antenna using standard 0.18-μm CMOS technology. IEEE Transactions on Antennas and Propagation. 2012;60(5):2234–2241. DOI: 10.1109/TAP.2012.2189725

[17] Yang F. and Rahmat-Samii Y., Electromagnetic band-gap structures in Antenna Engineering, 1st ed. The Cambridge RF and Microwave Engineering Series. Cambridge: Cambridge University Press; 2008. 282 p. DOI: 10.1017/CBO9780511754531

[18] Sohn J. R., Kim K. Y., Tae H.-S., and Lee H. J., Comparative study on various artificial magnetic conductors for low-profile antenna. Progress in Electromagnetics Research. 2006;61: 27–37. DOI: 10.2528/PIER06011701

[19] Barakat A., Allam A., Elsadek H., Abdel-Rahman A. B., Pokharel R. K., Bisognin A., and Luxey C., 60 GHz CMOS circular patch AoC on modified asymmetric AMC. Microwave Journal. Forthcoming.

[20] Cohn S. B., Electrolytic-tank measurements for microwave metallic delay-lens media. Journal of Applied Physics. 1950;21:674–680. DOI: 10.1063/1.1699730

[21] Clavijo S., Diaz R. E., and McKinzie W. E., Design methodology for Sievenpiper high-impedance surfaces: an artificial magnetic conductor for positive gain electrically small antennas. IEEE Transactions on Antennas and Propagation. 2003;51(10):2678–2690. DOI: 10.1109/TAP.2003.817575

[22] Zeghbroeck B. V., Principles of Semiconductor Devices and Heterojunctions. 1st ed. New Jersey: Prentice Hall; 2009. 450 p.

[23] Barakat A., Allam A., Elsadek H., Abdel-Rahman A. B., Pokharel R. K., and Kaho T., Improved gain 60 GHz CMOS antenna with N-well grid. IEICE Electronics Express. 2016; 13(5): 20151115. DOI: 10.1587/elex.13.20151115

[24] Park J., Mun G., Yu D., Lee B., and Kim W. N., Proposal of simple reference antenna method for EMI antenna calibration. In: IEEE International Symposium on Electromagnetic Compatibility (EMC); 14–19 August; Long Beach, CA, USA. USA: IEEE; 2011. p. 90–95. DOI: 10.1109/ISEMC.2011.6038290

[25] Titz D., Ferrero F., and Luxey C., Development of a millimeter-wave measurement setup and dedicated techniques to characterize the matching and radiation performance of probe-fed antennas. IEEE Antennas and Propagation Magazine. 2012; 54(4):188–203. DOI: 10.1109/MAP.2012.6309179